Electrodeposition of Bi films on H covered n-GaAs(111)B substrates

Alicia Prados and Rocío Ranchal

Dpto. Física de Materiales, Universidad Complutense de Madrid. Ciudad Universitaria s/n, Madrid 28040, Spain

*Corresponding author: a.prados@ucm.es Phone: (+34) 91 394 5012;

Fax: (+34) 91 394 4547

Abstract

We have investigated how the presence of an adsorbed hydrogen layer affects the nucleation and properties of Bi layers grown by dc electrodeposition at different overpotentials on n-GaAs(111)B substrates with a carrier concentration of $1.3 \cdot 10^{17}$ cm^{-3} in darkness and at 300 K. The kinetics of Bi(III) ions reduction is controlled by the overpotential but also negatively affected by the adsorbed hydrogen layer, as deduced from the deconvolution of the current density transients recorded during the nucleation of the films. The surface morphology and the structural properties of the Bi films are correlated with the nucleation process and therefore, influenced by both the overpotential and the adsorbed hydrogen layer. At low overpotentials, porous and rough Bi films with a low crystal quality are obtained due to the low rate of proton and Bi(III) ion reduction. As the overpotentials raises, the rate of these reactions increase leading to flatter and more compact Bi films with a higher crystal quality. The electrical properties of the Bi/n-GaAs interface depend on the interfacial states whose origin is again the combined effect of the adsorbed hydrogen layer and growth overpotential.

Keywords

Bismuth; n-GaAs; Electrodeposition; Nucleation; Thermionic Emission.

1. Introduction

Bismuth (Bi) is a semimetal with interesting electronic properties at the nanoscale [1, 2, 3, 4, 5]. In a thin film configuration, Bi can be used in the development of new spintronic devices that take advantage of its surface states which are strongly spin-polarized via Rashba effect [6, 7]. In fact, a large spin to charge conversion induced by spin–orbit coupling in a Bi/Ag Rashba interface has been very recently observed [8]. Consequently, in order to investigate the possibility of implementing Bi in new applications, it is compulsory to deeply investigate the growth of Bi thin films.

Among the different growth techniques, electrodeposition appears as the most suitable to grow Bi since it is a fast procedure to obtain high quality layers on different substrates ([9] and references therein). Also important to remark, it is a cost-effective growth method compatible with patterning and transferable to industry. In order to implement Bi in electronic devices, semiconductors like GaAs can be very versatile for several reasons. Tunnel [10, 11] or rectifying [12] Schottky barriers can be obtained by varying the substrate doping level, leading to different mechanisms for electron transport through the interface, thermionic-field emission or thermionic emission, respectively. Moreover, modifying the substrate surface orientation it is possible to synthesize Bi thin films with different crystalline textures and interfacial electrical properties [10]. Therefore, a wide range of devices could be fabricated starting from just one material and growth technique. However, one of the main drawbacks of the electrodeposition of Bi onto n-GaAs is the presence of a blocking layer of adsorbed hydrogen (H_{ads}) at the substrate surface. This blocking layer results from the interaction between the n-GaAs surface states and the protons (H^+) of the electrolyte. Although it might protect the n-GaAs surface from oxidation, it will hinder the nucleation of Bi(III) ions avoiding the growth of compact and high quality Bi thin films [13]. To solve this problem, we designed a procedure that desorbs the H_{ads} layer before performing the growth of the Bi layer,

so high-quality films can be obtained [14, 10, 11]. Nevertheless, this protocol involves the dissolution of an initial Bi deposit and, therefore, it can only be used with highly-doped semiconducting substrates with a carrier concentration higher than $2\cdot10^{17}$ cm^{-3}. For n-GaAs substrates with a lower carrier concentration, that we will call from now on “lower-doped n-GaAs”, we investigated other protocols based on the electrodeposition of Bi under illumination conditions [14] since photogenerated holes remove the H_{ads} layer [15]. However, this cannot be used because illumination also produces the photocorrosion of the n-GaAs surface [16, 17, 18]. Considering the experimental results reported so far, we can only conclude that the electrodeposition of Bi thin films on lower-doped n-GaAs substrates has to be performed in the presence of the H_{ads} layer and therefore, it is necessary to explore the optimum growth conditions to achieve high quality Bi thin films.

We showed the strong impact that the growth overpotential has on the properties of Bi layers electrodeposited at constant potential on H_{ads}-free highly doped n-GaAs(111)B substrates [11, 9]. We reported that the morphological, structural and interfacial electrical properties are clearly correlated with the nucleation process which is in turn correlated with the energy band diagram of the semiconductor-electrolyte interface (SEI). Here, it is not possible to remove the H_{ads} layer, so the effect of the growth overpotential on the nucleation of the Bi films is affected by the presence of this layer. Consequently, the goal of the present work is double: i) to study in detail the combined effect of the growth overpotential and the H_{ads} layer on the nucleation and properties of Bi films electrodeposited at dc potentials on H_{ads}-covered lower-doped n-GaAs(111)B substrates, and ii) to find the optimal conditions to achieve high quality Bi thin films on these substrates. We have also analyzed the effect of the growth mode (static or dynamic) on the properties of the Bi layer.

2. Experimental

Electrochemical experiments have been carried out using a stable water-based electrolyte containing 1 mM Bi_2O_3 (bismuth oxide) as the Bi(III) cation source and 1 M $HClO_4$ (perchloric acid) as supporting electrolyte. Solutions were prepared with analytical grade chemicals and deionized water in order to avoid free ions. Bismuth oxide was first added to perchloric acid in a volumetric flask, and then, the solution was made to the mark with deionized water. The pH of the solution (approximately 0.1) was not necessary to be further adjusted. Working electrodes were Si doped n-type GaAs(111)B wafers, supplied by Semiconductor Wafer Inc., with a carrier concentration of $n = 1.3 \times 10^{17}$ cm^{-3}. Ohmic contacts were made on the back of the wafers by thermal evaporation of 80 nm of AuGe (2% Ge) and 250 nm of Au, followed by an annealing at 380 ºC in forming gas for 90 s. The total surface area exposed to the electrolyte was 0.15 cm^2 in all cases. Prior to each experiment, substrates were degreased and then etched to remove GaAs native oxide under darkness conditions. First, substrates are dipped in a solution of HCl (10% vol.) for 2 min to remove arsenic and gallium oxides [19]. Then, substrates are rinsed in deionized water for 2 min to remove Ga-Cl_x species since they are soluble in water [20]. Finally, substrates are immersed in 1 M $HClO_4$ (supporting electrolyte) for 2 min to remove possible Cl^- ions remaining in the solution or adsorbed at the substrate surface. Then, the substrate surface is protected from air with a drop of 1M $HClO_4$ (supporting electrolyte) when transferred to the Bi(III) solution, where substrates remained 2 min to reach a stable open-circuit potential (OCP). In this condition, the substrate surface is oxide-free with about one monolayer coverage of elementary As that interacts with the protons in the solution (As-H) [21], creating a layer of adsorbed hydrogen [13]. Electrochemical experiments were controlled by a PalmSens EmStat3+Blue potentiostat and carried out in a three-electrode cell with a platinum mesh as counter electrode and a Ag/AgCl (3 M NaCl) reference electrode supplied by BASi ($E_{eq} =$ 0.196 V vs. SHE). In this

study, all potentials are referred to this electrode. All electrochemical experiments were performed without agitation, at 300 K and in darkness. After deposition, films were rinsed in deionized water and dried with N_2.

Surface characterization was done by means of a Nanoscope Atomic Force Microscope (AFM) with a Si tip, working in tapping mode and operating in air. The surface roughness has been characterized by the root mean square (rms) obtained from the images analyzed with WSxM 5.0 software and Nanoscope 5.31r1 software. Structural characterization of the Bi layers was done by X-Ray Diffraction (XRD) using a Philips X'Pert PRO system equipped with a Cu target ($\lambda_{K\alpha}$ = 1.54 nm) and a four-circle goniometer. All films were measured in a symmetric Bragg-Brentano configuration ($\theta - 2\theta$ scan) to determine the preferred orientation of the films. To avoid substrate reflections, an offset of 0.5^{o} was introduced between the incidence and the diffracted direction ($\omega = \theta - \theta_{offset}$). The crystallographic uniformity of the Bi layers has been analyzed by means of ω-rocking curves and ϕ-scans (azimuthal scans). The full width at half maximum (FWHM) of these curves is twice the average tilt and twist of Bi grains with respect the GaAs substrate, respectively. In order to extract the FWHM values with their corresponding errors, the ω-rocking curves have been fitted to a pseudovoigt function and the ϕ-scans to a Gaussian function. The values obtained for the FWHM have been corroborated with the software X'Pert Data Viewer provided by PANalytical B. V.

Finally, the Bi/GaAs interface was characterized electrically by means of current density-voltage (j-V) curves. Several diodes with 230 μm and 250 μm of diameter were fabricated in the Bi films by standard optical lithography followed by photochemical etching. Afterward, an electrical contact made by 20 nm Cr/300 nm Au was evaporated on the top of the Bi diodes to protect them. I-V measurements were carried out at 290 K in a Janis probe station (model CCR10-1) with a Hewlett Packard 4145 semiconductor parameter analyzer.

All diodes show a good reproducibility for the measured curves. At least 10 diodes have been measured in each sample, giving standard errors below 6%.

3. Results

4.1. Electrochemical characterization

Figure 1 shows a cyclic voltammetry (CV) performed at 10 mV/s on an n-GaAs substrate immersed in the Bi(III) solution. The CV comprises two scans and starts at the OCP ≈ 70 mV, goes first toward the cathodic, then to the anodic stage and finishes at the initial OCP. In the first scan we can observe a cathodic peak with an onset potential (defined as the intersection of the rising current of the cathodic peak with respect to its baseline) around -200 mV, whereas the second scan presents a reduction peak with a different shape and a more positive onset potential (≈ -100 mV). Taking into account our previous work, these two peaks consist of the superposition of those assigned to Bi(III) ion and H^+ reduction on the n-GaAs surface [13, 10, 9]. Despite the reduction peaks, no anodic peak is observed in the CV, i.e., the metallic Bi cannot be oxidized into Bi(III) ions during the anodic stage (inset Figure 1).

Continuing with the electrochemical characterization, we have studied the effect of the growth potential on the nucleation of 40 nm thick Bi layers. The analysis of the current density transients obtained at different overpotentials has proven to be a powerful tool for visualizing all the processes that occur during the nucleation of the Bi films and the competition between them. Therefore, current density transients have been recorded during the nucleation of the films at four different cathodic potentials: -0.25 V, -0.3 V, -0.45 V and -0.7 V (Figure 2a). Due to the similarities between the SEI and a Schottky barrier [22, 23, 24], it is useful to define the overpotential of the SEI (η_{SEI}) as the bias voltage applied to it, i.e., the potential applied to the n-GaAs substrate (E) measured with respect to its equilibrium potential (OCP): $\eta_{SEI} = E - OCP$. Thus, in our analysis we will use the overpotentials equivalent to the applied cathodic potentials: -0.32 V, -0.37 V, -0.52 V and -0.77 V. We have

analyzed the current density transients by a procedure developed by Palomar-Pardavé *et al.* [25] that allows the deconvolution of the current density, $j(t)$, into its individual contributions, j_i (with i = *SEI, des, ads, PR* and *3D*), each one assigned to a different process. This procedure consists in a nonlinear fit of the experimental $j(t)$ to a theoretical nucleation model, using the Marquardt–Levenberg algorithm. For cathodic reactions, where the current density is negative, the absolute value of $j(t)$ should be used. We have elaborated a theoretical nucleation model based on several processes that occur in the SEI when it is biased, and that accurately describes the experimental nucleation curves for the electrodeposition of Bi on n-GaAs substrates [9]:

[a] Charging of the SEI capacitance considering it as a series RC circuit [24]:

$$j_{SEI}(t) = \frac{Q_{SEI}}{\tau_{SEI}} \cdot exp\left(-\frac{t}{\tau_{SEI}}\right) \tag{1}$$

[b] Desorption of OH^- and ClO_4^- anions:

$$j_{des}(t) = \frac{Q_{des}}{\tau_{des}} \cdot exp\left(-\frac{t}{\tau_{des}}\right) \tag{2}$$

[c] Adsorption of H^+ via surface states on available surface sites present at the GaAs electrode [14]:

$$j_{ads}(t) = \frac{Q_{ads}}{\tau_{ads}} \cdot exp\left(-\frac{t}{\tau_{ads}}\right) \tag{3}$$

The parameters Q_{SEI}, Q_{des} and Q_{ads} represent the electrical charge involved in each process, and τ_{SEI}, τ_{des} and τ_{ads} represent their time constants [26].

[d] Reduction of H^+ on the GaAs surface:

$$j_{PR} = z_{PR} \cdot F \cdot k_{PR} \tag{4}$$

where z_{PR} is the number of electrons involved in the reduction reaction; F is Faraday's constant; and k_{PR} is the rate constant of the reaction [27]. This expression takes into account the two steps involved in the hydrogen evolution reaction, which follows the Volmer-Heyrovsky route on GaAs surfaces in acidic aqueous solutions [28].

[e] Reduction of Bi(III) ions into metallic Bi following a 3D nucleation controlled by diffusion, and delayed by an induction time, t_0, associated with the initial current decay [29]. This process can be described by the following expression:

$$j_{3D}(t) = P_4 \cdot (t - t_0)^{-1/2} \cdot \theta(t - t_0) \tag{5}$$

where $\theta(t)$ is the n-GaAs surface area covered by the diffusion zones of Bi nuclei [30].

$$\theta(t) = 1 - exp\left\{-P_2 \cdot \left[(t - t_0) - \frac{(1 - exp[-A \cdot (t - t_0)])}{A}\right]\right\} \tag{6}$$

and

$$P_2 = N_0 \cdot \pi \cdot D \cdot \left(\frac{8\pi \cdot c_0 \cdot M}{\rho}\right)^{1/2} \tag{7}$$

$$P_4 = \left(\frac{z \cdot F \cdot D^{1/2} \cdot c_0}{\pi^{1/2}}\right) \tag{8}$$

where A, D and c_o are the nucleation frequency per active site, the diffusion coefficient, and the concentration in the bulk of the electrolyte of Bi(III) ions, respectively; M and ρ are the molar mass and the density of metallic Bi; and N_o is the saturation density of nucleation active sites on the GaAs surface. To fulfill the requirement of dimensional homogeneity, c_o should be introduced in mol·cm^{-3} and ρ in g·cm^{-3}.

The nucleation process is divided into two regimes delimited by the induction time, t_0 [9]. During the first regime the SEI is rearranged due to the modification of the potential from the OCP to the growth potential. When the second regime starts, the Bi(III) ion reduction (j_{3D}) begins and the GaAs surface is progressively covered by metallic Bi. This new process alters H^+ reduction (j_{PR}) since the two reactions occur via conduction band electrons [31, 28]. However, H^+ adsorption (j_{ads}) can run in parallel to Bi(III) ion reduction because they take place at different surface sites and through different electronic states [26, 32]. Therefore, our nucleation model is described by the following equations:

$$j(t) = j_{SEI}(t) + j_{des}(t) + j_{ads}(t) + j_{PR} \qquad t \leq t_0 \tag{9}$$

$$j(t) = j_{ads}(t) + j_{PR} \cdot [1 - \theta(t)] + j_{3D}(t) \qquad t > t_0 \tag{10}$$

The details of this model are fully reported in reference [9]. In order to obtain accurate and reliable results, the experimental transients shown in Figure 2a have been fitted to eq. 9 and 10 computing the value, the standard error, and the lower (LCL) and upper (UCL) 95% confidence limits of the parameters Q_{SEI}, τ_{SEI}, Q_{des}, τ_{des}, t_0, Q_{ads}, τ_{ads}, k_{PR}, D, A, and N_0. Table 1 contains the best-fit parameters with their respective errors obtained on basis of the 95% confidence limits. All fittings can be considered accurate since relative errors are below 7 %.

Table 1. Best-Fit Parameters and Their Errors Obtained from the Analysis of the Experimental Current Density Transients Shown in Figure 2a.

η_{SEI} (V)	-0.32	-0.37	-0.52	-0.77
τ_{SEI} (ms)	(7.49 ± 0.38)	-	-	-
Q_{SEI} (μC·cm^{-2})	(0.302 ± 0.023)	-	-	-
τ_{des} (ms)	(44.0 ± 2.0)	(5.66 ± 0.14)	(0.785 ± 0.016)	-
Q_{des} (μC·cm^{-2})	(1.825 ± 0.071)	(2.103 ± 0.055)	(3.13 ± 0.10)	-
t_0 (ms)	(2951.6 ± 1.3)	(628.9 ± 3.2)	(5.13 ± 0.18)	(2.491 ± 0.021)
τ_{ads} (ms)	(208.8 ± 2.4)	(65.81 ± 0.63)	(5.265 ± 0.088)	(3.969 ± 0.020)
Q_{ads} (μC·cm^{-2})	(9.867 ± 0.073)	(22.50 ± 0.12)	(20.33 ± 0.18)	(101.10 ± 0.52)
k_{PR} (·10^{-10} mol·cm^{-2}·s^{-1})	(5.1600 ± 0.0011)	(12.946 ± 0.016)	(140.27 ± 0.54)	(410.1 ± 1.8)
D (·10^{-8} cm^2·s^{-1})	(1146.24 ± 0.49)	(1261.77 ± 0.55)	(966.65 ± 0.46)	(1110.79 ± 0.35)
A (s^{-1})	(0.5589 ± 0.0011)	(12.80 ± 0.41)	(17.3 ± 1.1)	(739 ± 21)
N_o (·10^5 cm^{-2})	(1.0423 ± 0.0014)	(1.1753 ± 0.0023)	(209.3 ± 6.7)	(761.7 ± 5.0)

Figure 2b-e shows the deconvolution of the experimental transients plotted in Figure 2a into their individual contributions according to the best-fit parameters listed in Table 1. It can be noticed that our theoretical model accurately describes all the transients except the minima of those obtained at lower η_{SEI} (-0.32 V and -0.37 V). This is a consequence of considering the SEI as a RC series circuit (eq. 1) when it is actually more complex.

4.2. *Morphological and structural characterization*

Figures 3a-e show AFM images obtained in each Bi film whereas Figure 3.f exhibits the evolution of the films rms with the overpotential. In all cases, the rms of the films is higher than that obtained for Bi films grown on H_{ads}-free highly doped n-GaAs substrates [11], and decreases with η_{SEI}. At low overpotentials (η_{SEI} = -0.32 V and -0.37 V), porous Bi layers with rounded islands and a rms of around 9-10 nm are obtained (Figure 3a-b and f). For η_{SEI} = -0.52 V and -0.77 V, the Bi films are more compact and present a higher coalescence and a lower rms (Figure 3c-d and f). At η_{SEI} = -0.77 V there is also a change of surface morphology, with the appearance of bigger round-shaped isolated islands. Since it is not possible to avoid the effect of the H_{ads} layer on the dc electrodeposition (static growth) on lower-doped n-GaAs substrates, we have explored the possibility of growing a Bi film in a dynamic mode, by performing consecutive CV scans. In order to obtain a 40 nm-Bi thick film, it is necessary to carry out 5 scans similar to those shown in Figure 1b. The Bi film grown in the dynamic mode (Figure 3e) presents a morphology similar to the film grown at η_{SEI} = -0.52 V (Figure 3c), although the latter is more compact and has a slightly lower rms (Figure 3f).

Figure 4 show the XRD diffraction patterns obtained in each Bi film. All the layers exhibit a (012) texture assigned to the rhombohedral structure of metallic Bi ($R\bar{3}m$, 166). This crystal texture is correlated with the substrate surface orientation and is independent of the growth overpotential, in agreement with previous work [10, 11]We have not found traces of oxides or secondary compounds.

Figure 5 show the FWHM obtained from the ω-rocking curves and the ϕ-scans. The ω-rocking curves give information about the out-of-plane crystal uniformity, and their FWHM is considered twice the average tilt of the Bi grains with respect to the GaAs surface. These scans have been performed around the Bi(024) Bragg reflection instead of the Bi(012) because the GaAs(111) reflection interferes with the latter, whereas the GaAs(222) reflection

does not interfere with the Bi(024). The ϕ-scans give information about the in-plane crystal uniformity, and their FWHM is considered twice the average twist of the Bi grains with respect to the GaAs surface. These scans are performed around the strongest asymmetric-Bragg reflections, i.e., reflections that are not related to the layer texture. In this case of Bi(012) films grown on GaAs(111)B, we have chosen the Bi(110) reflection, which has a 3-fold symmetry. However, the azimuthal scans show 12 reflections, which indicates that Bi grains are distributed in four possible orientations with respect to GaAs(111)B planes. From the data in Figure 5 we can infer that all the Bi layers show a lower crystal quality than those grown on H_{ads}-free highly doped n-GaAs substrates [11]. The out-of plane crystal quality is enhanced with η_{SEI} whereas the in-plane crystal quality is less sensitive to the growth overpotential taking into account the error bars. Similarly to the morphology, the film grown in the dynamic mode exhibits an out-of-plane quality between that of the films grown at η_{SEI} = -0.37 V and -0.52 V.

4.3. Electrical characterization of the interface

Figure 6a shows *j-V* curves measured in each Bi film. In all cases, the reverse current density is 6 orders of magnitude lower than the forward current density, indicating a good rectifying behaviour, i.e., there is no significant electron tunneling through the barrier. Consequently, the *j-V* curves should be analyzed on the basis of Thermionic Emission (TE) theory [33]. Then, the current that flows through the Schottky barrier is described by:

$$j = A^{**}T^2 \cdot exp\left(-\frac{q\phi_B}{k_B T}\right) \cdot \left[-1 + exp\left(\frac{qV_D}{k_B T}\right)\right] \quad (11)$$

where A^{**} is the modified Richardson constant, T is the temperature, q is the elementary charge, ϕ_b is the potential barrier height, k_B is Boltzmann constant and V_D is the potential across the Schottky barrier. The modification of Richardson constant, A^*, into $A^{**} = f_p \cdot f_q \cdot A^*$ takes into account the probability of an electron reaching the metal without being backscattered (f_p) and the quantum-mechanical transmission (f_q) [33]. The optimal value for

GaAs substrates is $A^{**} = 3 \cdot 10^4$ A m^{-2} K^{-2}, which has been experimentally evidenced [34]. V_D can be extracted from the applied bias, V, by modeling the system like a Schottky diode in series with a resistor of resistance R. This R represents the effect of the bulk of the semiconductor, the electrical contacts, and the probes used to perform the measurements. Consequently:

$$V_D = (V - j \cdot S \cdot R) \tag{12}$$

where S is the area of the diode. In order to obtain a good fit it is necessary to suppose the existence of interfacial states at the Bi/n-GaAs interface [33]. It is usually considered that these states, with a density D_{SS}, are located at an interfacial layer of thickness d. Since the XRD measurements do not show traces of oxides or other compounds, these interfacial states must be related to metal-induced gap states (MIGS) or to interfacial defects that act as charge traps. Although the principal native defect that exerts a strong influence on the electrical properties of GaAs Schottky barriers is the As_{Ga} antisite [35], additional interfacial defects could be introduced by the mismatch between the Bi layer and the GaAs surface (Figure 5). Due to the presence of these interfacial states, the barrier height presents a dependence on the applied field, i.e., on the applied bias:

$$\phi_b = \phi_b^0 + \frac{\phi_1}{2} - \left\{\phi_1 \cdot \left(\phi_b^0 + \frac{\phi_1}{4} - V_D - \frac{E_C - E_F}{q} - \frac{k_B T}{q}\right)\right\} \tag{13}$$

where ϕ_b^0 is the zero-bias barrier height, ϕ_1 is a parameter related to the characteristics of the interfacial states layer, E_c is the energy of the bottom of the conduction band (CB) and E_F is the Fermi energy level. Considering the bulk carrier concentration of our substrates ($n = 1.3 \times 10^{17}$ cm^{-3}) and using the Nilsson approximation [36]:

$$E_C - E_F = -k_B T \cdot \left\{ \frac{ln(u)}{1-u^2} + \frac{\left(\frac{3}{4}\sqrt{\pi} \cdot u\right)^{\frac{2}{3}}}{1 + \left[0.24 + 1.08 \cdot \left(\frac{3}{4}\sqrt{\pi} \cdot u\right)^{\frac{2}{3}}\right]^{-2}} \right\} \tag{14}$$

where the parameter u is defined as:

$$u = F_{\frac{1}{2}}(\eta) = \frac{n}{N_C} \tag{15}$$

Taking into account N_c (= $4.7\cdot10^{17}$ cm^{-3}) the effective density of states for electrons in the CB in GaAs at 290 K [37] and $F_{1/2}(\eta)$ the Fermi-Dirac integral [36], we obtain a value of E_C - $E_F \approx 26$ meV. The parameter ϕ_1 is:

$$\phi_1 = \frac{2\alpha^2 qn}{\varepsilon_s} \tag{16}$$

where ε_s is the semiconductor dynamic electrical permittivity, which is $10.89\cdot\varepsilon_0$ for GaAs [38], being ε_0 the vacuum permittivity. The parameter α is related to the characteristics of the layer containing the interfacial states:

$$\alpha = \frac{d\varepsilon_s}{\varepsilon_i + qdD_{ss}} \tag{17}$$

Since this layer is not related to the formation of a new phase, we have considered its electrical permittivity as $\varepsilon_i = \varepsilon_0$. The zero-bias barrier height is also related to the interfacial states through the Bardeen model [33]:

$$q\phi_b^0 = \gamma \cdot q(\phi_m - \chi) + (1-\gamma)\cdot(E_g - \phi_0) \tag{18}$$

where ϕ_m is the metal work function (4.35 V for Bi) [37], χ is the semiconductor electron affinity (4.07 V for GaAs) [37], E_g is the semiconductor band gap (1.42 eV for GaAs) [37] and ϕ_0 is the neutral energy level for the interfacial states (0.5 eV for GaAs) [39, 33, 40]. The parameter γ is also related to the characteristics of the layer containing the interfacial states [33]:

$$\gamma = \frac{\varepsilon_i}{\varepsilon_i + qdD_{ss}} \tag{19}$$

All j-V curves have been analyzed by a nonlinear fit of the experimental data to eq. 11 using the Marquardt–Levenberg algorithm, with R, D_{ss} and d as free parameters. Their uncertainties have been provided by the fitting on basis of the 95% confidence limits. The

fitting has been limited from 0.45 V to -0.3 V because at higher bias there are additional effects such as local heating [41]. Figure 6b shows two experimental *j-V* curves with their respective fittings. Table 2 lists the weighted average values of *R, d* and D_{SS} obtained for each Bi film. The errors have been calculated taking into account the errors provided by the weighted average and the standard deviation. From *d* and D_{SS}, the zero-bias barrier height, ϕ_b^0, has been obtained according to eq. 18 and 19 and its error has been calculated by propagation of uncertainties [42]. All these values can be considered accurate since their relative errors are lower than 6%, except for *R* which has relative errors up to 30%.

Table 2. Resistance (*R*), Interfacial Layer Width (*d*), Density of Interfacial States (D_{SS}) and Zero-Bias Barrier Height ($q\phi_b^0$) Values with their Respective Uncertainties obtained by *j-V* Curves Performed in the Bi Films.

η_{SEI} (V)	*R* (Ω)	*d* (nm)	D_{SS} ($\cdot 10^{16}$ eV^{-1} m^{-2})	$q\phi_b^0$ (eV)
-0.32	4.75 ± 0.68	4.06 ± 0.12	8.410 ± 0.098	0.8307 ± 0.0027
-0.37	5.2 ± 1.5	4.06 ± 0.25	7.01 ± 0.25	0.8158 ± 0.0071
-0.52	4.8 ± 0.8	3.79 ± 0.11	8.51 ± 0.23	0.8263 ± 0.0034
-0.77	9.25 ± 0.91	3.802 ± 0.050	9.406 ± 0.047	0.8343 ± 0.0012
CV	21.3 ± 4.7	3.85 ± 0.14	9.32 ± 0.11	0.8346 ± 0.0033

4. Discussion

4.1. Energy band diagram of the SEI

As we already reported, the electrochemical properties of a SEI are closely related to its energy band diagram [9]. Therefore, it is useful to show briefly the principal characteristics of this diagram. Although a SEI can be a complex structure, it is possible to establish some analogies with a Schottky barrier where the metal role is played by the Bi(III) electrolyte and the interfacial states are the surface states at the n-GaAs electrode (Figure 7) [22, 23, 24]. The

position of the CB edge at the SEI can be derived from the experimental flat band potential [9]. Taking into account the flat band potentials of n-GaAs electrodes reported in several articles [43, 44, 32, 21, 45, 18], we have calculated the average value of the CB edge:

$$E_{C,s} = (-3.737 \pm 0.020)\ \text{eV} \quad (20)$$

The uncertainty has been considered as the standard deviation of the average due to the different reported values. In the same way we have calculated the valence band (VB) edge:

$$E_{V,s} = E_{C,s} - E_g = (-5.157 \pm 0.020)\ \text{eV} \quad (21)$$

The surface states of the GaAs are formed by a surface band of intrinsic states (SS_{int}) located near the VB and related to surface dangling bonds [46], and some discrete extrinsic states (SS_{ext}) associated to surface defects. [40] According to the Advanced Unified Defect Model (AUDM) the most relevant SS_{ext} in GaAs are antisites [35]. The As_{Ga} antisite (an As atom surrounded by four As atoms) is a double donor whose energy levels are located at both 0.5 + $E_{V,s}$, and 0.75 eV + $E_{V,s}$. The Ga_{As} antisite (a Ga atom surrounded by four Ga atoms) is a double acceptor that provides two energy levels between the lower level of the As_{Ga} antisite and $E_{V,s}$. These native defects have a great importance in GaAs Schottky barriers since they are related to the pinning of the Fermi level (E_F). [40] The position of the E_F at the SEI in equilibrium conditions can be obtained from the OCP. In our case, OCP ≈ 0.07 V vs Ag/AgCl, which is equivalent to -4.77 eV with respect to the vacuum level [22]. The position of the E_F approximately coincides with the energy of the highest occupied level of SS_{int}, measured by photocapacitance spectroscopy ($E_1 = E_{C,s} - 0.98$ eV) [47]. This indicates that surface dangling bonds are filled, i.e., saturated by adsorbed species, which is the reason for the absence of surface reconstructions in liquid media [46]. Depending on the type of adsorbed ion at the surface, the OCP can slightly vary from 70 mV (adsorbed protons) to 100 mV (adsorbed anions) due to the different effect that each type of ion produces on the surface

dipole [10]. At OCP conditions, i.e., in equilibrium, the energy bands of the n-GaAs electrode bend upwards, leading to a contact potential (V_{bi}):

$$qV_{bi} = E_{C,s} - E_C = \left(E_{C,s} - E_F\right) + \left(E_F - E_C\right) \approx 0.94\ eV \quad (22)$$

where and E_C - E_F is obtained from eq. 14. Associated to V_{bi}, a space charge region (SCR) of width w is formed in the near-surface region of the n-GaAs electrode:

$$w = \sqrt{\left(\frac{2\varepsilon_S}{q \cdot N_D^+}\right) \cdot \left(V_{bi} + \eta_{SEI} - \frac{k_B T}{q}\right)} \quad (23)$$

where N_D^+ is the concentration of the ionized donors (equal to the bulk electron concentration, n). At OCP conditions (η_{SEI} = 0 V), w = 100 nm. This SCR contains a certain positive charge assigned to the ionized donors that electrically interact with the electrolyte, affecting the structure of the electrical double layer. As abovementioned, the Bi(III) electrolyte plays the role of the metal in a Schottky barrier although composed of several energy levels instead of one. These energy levels, one per redox couple, present a Gaussian distribution due to the effect of the water molecules surrounding the ions [22]. When E_F lies above one of these energy levels, electrons can be transferred from the substrate to the electrolyte promoting the reduction reaction [22, 23].

4.2. Analysis of the CV and the current-density transients

When translated to the energy band diagram (Figure 7), the CVs shown in Figure 1 consist in moving E_F upwards (cathodic stage or forward bias) and then, downwards (anodic stage or reverse bias) with respect to its equilibrium position (OCP or zero bias). When the E_F surpasses the energy level of a redox couple a reduction peak is obtained. The reduction peak of the first scan has an onset potential similar to H^+ reduction potential ($E_{H^+/H_2} \approx -0.196\ V$) although Bi(III) ions reduction is activated at more positive potentials [48]. This results from the presence of the blocking H_{ads} layer on the n-GaAs surface [13]. Due to the absence of free surface sites, Bi(III) ions cannot get reduced on the n-GaAs surface until H^+ reduction is activated since this reaction frees surface sites [13, 10, 15]:

$$H^{+} + H_{ads} + e^{-} \rightarrow H_{2(g)} \quad (24)$$

Therefore, when using an H_{ads}-covered n-GaAs electrode, the reduction of Bi(III) ions can only occur simultaneously with H^+ reduction, which is activated below ≈ -200 mV, i.e., -4.5 eV in the energy scale (Figure 7). The absence of anodic peaks in the CVs is a consequence of the wide SCR provided by the low doping level of the n-GaAs substrate (eq. 23), which avoids the necessary electron tunneling from the electrolyte to the substrate for the anodic reaction to occur. This has two consequences: i) in the second scan of the CV Bi(III) ions get reduced on an n-GaAs surface partially covered by metallic Bi, which gives a reduction peak with a different shape and a different onset potential (≈ -100 mV), ii) it is not possible to perform the scan route described in reference [14] to obtain an H_{ads}-free n-GaAs surface on lower-doped substrates. As a result of the second point, the electrodeposition of the Bi layers is affected by the presence of the H_{ads} layer regardless of the η_{SEI}.

The analysis of the current-density transients obtained during the nucleation of the Bi films (Figure 2) has proven to be a powerful tool to gain insight into this combined effect. When a negative η_{SEI} is applied E_F moves upwards (Figure 7), modifying w (eq. 23) and the positive charge contained in the SCR. In order to maintain the electrical neutrality, the SEI is reorganized during the first stage of the transients (eq. 9). The charging of the SEI (j_{SEI}, red dashed line in Figure 2.b) is only detected at η_{SEI} = -0.32 V because of the used step time (t_{step} = 1 ms). The time constant (τ_{SEI}) and the charge (Q_{SEI}) involved in this process are similar to those obtained for a low overpotential (η_{SEI} = -0.25 V) in our previous work [9]. Anion desorption (j_{des}, blue dashed line in Figure 2.b-c) is significantly lower than that observed in H_{ads}-free n-GaAs substrates for similar η_{SEI} [9] indicating that the H_{ads} occupies an important percentage of the electrode surface. The amount of desorbed anions (Q_{des}) increases with η_{SEI} due to the decrease of w and, therefore, the decrease of the positive charge associated with it. The time constant, τ_{des}, decreases with the overpotential up to η_{SEI} = -0.52 V when the

desorption process becomes undetectable. The time required for the reorganization of the SEI is given by t_0, which is always higher than τ_{SEI} and τ_{des}. As well as these time constants, t_0 rapidly decreases with η_{SEI} as the SEI reorganization becomes faster (Table 1).

The dependence of H^+ adsorption (j_{ads}, green dashed line in Figure 2.b-e) with η_{SEI} is different from what it is observed on a H_{ads}-free n-GaAs surface [9] indicating that this process is influenced by the presence of the H_{ads} layer. Although Q_{ads} increases with η_{SEI} (Table 1), it is always lower than the charge associated with the formation of one monolayer of H_{ads}, q_m = 232 μC·cm^{-2}, reflecting that the n-GaAs surface is already covered by H_{ads}. In addition, the relation between Q_{des} and Q_{ads} indicates that H^+ gets adsorbed on the surface sites that become free after anions are desorbed. In fact, Q_{des} is always lower than Q_{ads} because of the bigger size of anions with respect to H^+. At η_{SEI} = -0.37 V there is an abrupt increase of Q_{ads} related to the coincidence of E_F with the As_{Ga} antisite upper level, when new *SS* become accessible (Figure 1.a). Although τ_{ads} always decreases with η_{SEI} (Table 1), it is lower than t_0 at low overpotentials (η_{SEI} = -0.32 V and -0.37 V), but similar or higher at high overpotentials (η_{SEI} = -0.52 V and -0.77 V). This is a consequence derived from the progressively enhancement of Bi(III) ion reduction (j_{3D}, orange line in Figure 2b-e), which delays H^+ adsorption at high η_{SEI}.

Protons reduction (j_{PR}, light blue dashed line in Figure 2b-e) is present in all transients and takes place even during the reorganization of the SEI due to the presence of H_{ads} on the n-GaAs surface. This process continues until all the n-GaAs surface is covered by metallic Bi, because Bi does not favor protons reduction [49]. From the comparison of k_{PR} obtained in this work with respect to a previous work where H_{ads}-free highly doped n-GaAs substrates were used [9], we can obtain two main conclusions. First, k_{PR} is lower in lower-doped substrates because the lower surface electron concentration decreases the reaction rates [22]. Second, the

increase of k_{PR} with η_{SEI} is more significant in H_{ads}-covered substrates because the presence of H_{ads} favors this reaction [32].

After the SEI is reorganized, Bi(III) ion reduction starts and the second range of the transients begins (eq. 10). The diffusion coefficient of Bi(III) ions, D, is not affected by the H_{ads} layer and has values between 1.6 to $2.6 \cdot 10^{-5}$ cm^{-2} s^{-1}, which are in the same magnitude of those found in the literature [50, 51, 52, 9]. Both the saturation density of nucleation sites, N_0, and the nucleation rate, A, are enhanced with η_{SEI} but do not show a clear dependence with it, i.e., the H_{ads} layer affects the two parameters. At low overpotentials (η_{SEI} = -0.32 V and -0.37 V), N_0 is small due to the blockade of the surface sites produced by the H_{ads} layer and the slow rate of H^+ reduction (Table 1). N_0 increases with η_{SEI} in all the studied range due to the enhancement of k_{PR}. A also increases with η_{SEI} but does not follow the exponential tendency reported in other work [53, 54, 55] or the dependency described by Sebastián *et al.* based on the classical theory of electrocrystallization [56]. At η_{SEI} = -0.37 V the value of A is higher than expected due to the coincidence of E_F with the As_{Ga} antisite upper level which raises Bi(III) ion reduction. Taking into account the data obtained with the analysis of the current density transients we can conclude that the principal SS_{ext} that influences on the electrochemical properties of an n-GaAs electrode is the upper level of the As_{Ga} antisite defect (0.75 eV + $E_{V,s}$). This result is in agreement with the recent work of M. Enache *et al.* [57] where they show that the principal group of electronic states at n-type GaAs electrodes is located at 0.7 eV below the bottom of the CB.

4.3. Properties of the Bi layers

All the studied films have a surface morphology (Figure 3a-e) in agreement with a 3D nucleation as expected from the analysis of the current density transients (Figure 2b-e). At low overpotentials (η_{SEI} = -0.32 V and -0.37 V), the blocking effect of the H_{ads} layer on Bi(III) ions reduction is significant due to the low k_{PR} and A (Table 1), leading to porous Bi layers

with a high rms (Figure 3a-b and f). It should be noticed that a more regular surface, with islands of similar sizes, is obtained at η_{SEI} = -0.37 V as a result of the higher *A* (Table 1). For η_{SEI} = -0.52 V and -0.77 V, H^+ and Bi(III) ions reduction are enhanced leading to more compact Bi films with a higher coalescence and a lower rms (Figure 3c-d and f). The appearance of bigger round-shaped isolated islands at η_{SEI} = -0.77 V can be related to the onset of water reduction (also considered as hydrogen evolution at high overpotentials) [9], reaction that alters the hydrodynamic conditions [58, 59]. Other authors have observed that this reaction has a clear impact on the surface morphology of electrodeposited films [60, 59]. Moreover, in the areas surrounding where the H_2 bubbles were formed, the composition of alloys [61] and the nanowires length [62] are altered. Due to the low overpotential of water reduction at a potential of *E* = -0.7 V, this reaction is undetectable in the deconvolution of the current-density transient shown in Figure 2e. In all cases the rms is higher than that obtained for Bi films grown on H_{ads}-free highly doped n-GaAs substrates [11], which is a result of the lower k_{PR} and *A* produced by the combination of the lower surface electron concentration and the presence of the H_{ads} layer. The morphology of the Bi film grown in the dynamic mode (Figure 3e) can be explained taking into account that the deposition rate in this growth is not constant but increases with the overpotential. Therefore, the most part of the Bi film is deposited at high η_{SEI} and, consequently, the morphology is similar to that obtained for Bi films grown at high dc potentials. However, since the CV starts at the OCP, the nucleation of the film occurs at low η_{SEI} which is responsible for the higher porosity of this film with respect to the film grown at η_{SEI} = -0.52 V (Figure 3c).

From the data in Figure 5 we can infer that the out-of plane crystal quality is mainly influenced by the overpotential and is enhanced progressively with η_{SEI}. At low η_{SEI} the presence of the H_{ads} layer combined with a low k_{PR} and a low *A* inhibits a good match between the Bi grains and the n-GaAs surface, leading to high crystal tilts (high FWHM/2).

As η_{SEI} increases, Bi(III) ion and H^+ reduction are enhanced leading to a better lattice match, i.e., lower tilts (lower FWHM/2). Nevertheless, the in-plane crystal quality remains constant through all the overpotentials, being only slightly enhanced at η_{SEI} = -0.77 V. Therefore, the in-plane crystal quality is mainly affected by the H_{ads} layer. Similarly to the morphology, the film grown in the dynamic mode exhibits both an out-of-plane and in-plane quality between the films grown at η_{SEI} = -0.37 V and -0.52 V because the nucleation takes place at low η_{SEI} but the main part of the film is deposited at high η_{SEI}. All the Bi layers show a lower crystal quality than those grown on H_{ads}-free highly doped n-GaAs substrates [11]. Similarly to the morphology, this results from the lower values of k_{PR} and A produced by the H_{ads} layer and the lower surface electron concentration.

All Bi/n-GaAs interfaces behave like Schottky barriers with a good rectifying behaviour. The values obtained for $q\phi_b^0$ are in good agreement with those found in the literature for n-GaAs Schottky barriers obtained by electrodeposition [31, 12, 63]. The dependence of $q\phi_b^0$ with η_{SEI} is similar to that obtained for Bi films electrodeposited on H_{ads}-free highly doped n-GaAs substrates [11]. Therefore, a similar explanation can be given. According to the MIGS model and the AUDM, the Fermi level at a Bi/n-GaAs Schottky barrier should be pinned at 0.5 eV above the VB [33, 40], which gives a $q\phi_b^0 = 0.92\ eV$. However, when MIGS are inhibited or the As_{Ga}/Ga_{As} antisites ratio is modified, E_F can be pinned at 0.75 eV above the VB, leading to a $q\phi_b^0 = 0.67\ eV$. This can happen when additional defects are created, for example, by the mismatch between the Bi layer and the n-GaAs surface or by the oxidation of the interface when the films are porous. Consequently, when the crystal quality of the Bi films is enhanced with η_{SEI} (Figure 5) the barrier height tends toward $q\phi_b^0 = 0.92$ eV (Table 2). However, at η_{SEI} = -0.32 V the barrier height increases despite its lower crystal quality because the porosity of the film allows the oxidation

of the interface when exposed to the air. Consequently, this interfacial oxide layer could incorporate new interfacial states that can store additional charge at the interface.

5. Conclusions

The main goal of this work has been to clarify the effect of the H_{ads} layer on the dc electrodeposition of Bi films at different overpotentials on lower-doped n-GaAs electrodes. We have also investigated its influence on the Bi properties. The effect of the H_{ads} layer on the nucleation of the Bi films can be elucidated from the deconvolution of the current density transients, especially from the behaviour of H^+ adsorption, H^+ reduction and Bi (III) ion reduction with η_{SEI}. In H_{ads}-covered n-GaAs substrates, Bi(III) ion reduction is always concurrent with H^+ reduction and consequently, the kinetics of the former is influenced by the kinetics of the latter. Bi films surface morphology is correlated with the nucleation process, principally through k_{PR} and A. As these two parameters are enhanced with η_{SEI}, flatter and more compact films are obtained when it increases. The in-plane crystal quality seems to depend just on the H_{ads} layer whereas the overpotential has an impact on the out-of-plane crystal quality. The electrical properties of the Bi/n-GaAs interface depend on the density of interfacial states, which are correlated with the crystal quality and the surface morphology of the Bi films. Comparing to Bi films grown on H_{ads}-free highly doped n-GaAs surface, we can conclude that both the low carrier density of the substrate and the presence of the H_{ads} layer lead to Bi films more porous and rough, with a lower crystal quality and lower Schottky barriers.

Acknowledgements

This work has been financially supported by the Spanish Ministry of Economy and Competitiveness (MINECO/FEDER) [project MAT2015-66888-C3-3-R]; Santander and Universidad Complutense de Madrid [project PR26/16-3B-2]. We would like to acknowledge

the postdoctoral fellowship granted by Comunidad de Madrid and the European Union [PEJD-2016/IND-2233]. We also acknowledge the use of facilities of Instituto de Sistemas Optoelectrónicos y Microtecnología (ISOM).

REFERENCES

[1] T. Hirahara, K. Miyamoto, A. Kimura, Y. Niinuma, G. Bihlmayer, E. V. Chulkov, T. Nagao, I. Matsuda, S. Qiao, K. Shimada, H. Namatame, M. Taniguchi, S. Hasegawa, Origin of the surface-state band-splitting in ultrathin Bi films: from Rasbha effect to a parity effect, New J. Phys. 10 (2008) 083038. DOI: 10.1088/1367-2630/10/8/083038.

[2] M. Wada, S. Murakami, F. Freimuth, G. Bihlmayer, Localized edge states in two-dimensional topological insulators: ultrathin Bi films, Phys. Rev. B 83 (2011) 121310(R). DOI: 10.1103/PhysRevB.83.121310.

[3] F. Y. Yang, K. Liu, K. Hong, D. H. Reich, P. C. Searson, C. L. Chien, Y. Leprince-Wang, K. Yu-Zhang, K. Han, Shubnikov-de Haas oscillations in electrodeposited single-crystal bismuth films, Phys. Rev. B 61 (2000) 6631-6636. DOI: 10.1103/PhysRevB.61.6631.

[4] C. A. Hoffman, J. R. Meyer, F. J. Bartoli, A. D. Venere, X. J. Yi, C. L. Hou, H. C. Wang, J. B. Ketterson, G. K. Wong, Semimetal-to-semiconductor transition in bismuth thin, Phys. Rev. B 48 (1993) 11431. DOI: 10.1103/PhysRevB.48.11431.

[5] S. Sangiao, J. M. Michalik, L. Casado, M. C. Martínez-Velarte, L. Morellón, M. R. Ibarra, J. M. De Teresa, Conductance steps in electromigrated Bi nanoconstrictions, Phys. Chem. Chem. Phys. 15 (2013) 5132. DOI: 10.1039/C3CP44133D.

[6] T. Hirahara, K. Miyamoto, I. Matsuda, T. Kadono, A. Kimura, T. Nagao, G. Bihlmayer, E. V. Chulkov, S. Qiao, K. Shimada, H. Namatame, M. Taniguchi, S. Hasegawa, Direct observation of spin splitting in bismuth surface states, Phys. Rev. B 76 (2007) 153305. DOI: 10.1103/PhysRevB.76.153305.

[7] A. V. Khvalkovskiy, V. Cros, D. Apalkov, V. Nikitin, M. Krounbi, K. A. Zvezdin, A. Anane, J. Grollier, A. Fert, Matching domain wall configuration and spin-orbit torques

for efficient domain-wall motion, Phys. Rev. B 87 (2013) 020402(R). DOI: 10.1103/PhysRevB.87.020402.

[8] J. C. Rojas Sánchez, L. Vila, G. Desfonds, S. Gambarelli, J. P. Attane, J. M. De Teresa, C. Magén, A. Fert, Spin-to-charge conversion using Rashba coupling at the interface between non-magnetic materials, Nat. Commun. 4 (2013) 2944. DOI: 10.1038/ncomms3944.

[9] A. Prados, R. Ranchal, Electrodeposition of Bi thin films on n-GaAs(111)B. I. Correlation between the overpotential and the nucleation process, J. Phys.Chem. C 122 (2018) 8874. DOI: 10.1021/acs.jpcc.8b01838.

[10] A. Prados, L. Pérez, A. Guzmán, R. Ranchal, Mixed effects of the atomic arrangement and surface chemistry on the electrodeposition of Bi thin films on n-GaAs substrates, J. Phys. Chem. C 120 (2016) 28295. DOI: 10.1021/acs.jpcc.6b09144.

[11] A. Prados, R. Ranchal, Electrodeposition of Bi thin films on n-GaAs(111)B. II. Correlation between the nucleation process and the structural and electrical properties, J. Phys. Chem. C 122 (2018) 8886. DOI: 10.1021/acs.jpcc.7b12263.

[12] Z. L. Bao, K. L. Kavanagh, Epitaxial Bi/GaAs diodes via electrodeposition, J. Vac. Sci. Technol. B 24 (2006) 2138. DOI: 10.1116/1.2218874.

[13] A. Prados, R. Ranchal, L. Pérez, Blocking effect in the electrodeposition of Bi on n-GaAs in acidic electrolytes, 143 (2014) 23. DOI: 10.1016/j.electacta.2014.07.137.

[14] A. Prados, R. Ranchal, L. Pérez, Strategies to unblock the n-GaAs surface when electrodepositing Bi from acidic solutions, Electrochim. Acta 174 (2015) 264. DOI: 10.1016/j.electacta.2015.05.188.

[15] B. H. Erné, F. Ozanam, J. -N. Chazalviel, The mechanism of hydrogen gas evolution on GaAs cathodes elucidated by in situ snfrared spectroscopy, J. Phys. Chem. B 103 (1999) 2948. DOI: 10.1021/jp984765t.

[16] H. Gerischer, Electrochemical behaviour of semiconductors under illumination, J. Electrochem. Soc. 113 (1966) 1174. DOI: 10.1149/1.2423779.

[17] J. Li, L. M. Peter, Surface recombination at semiconductor electordes. Part IV., J. Electroanal. Chem. 199 (1986) 1. DOI: 10.1016/0022-0728(86)87038-3.

[18] Y. Huang, J. Luo, D. G. Ivey, Comparative study of GaAs corrosion in H_2SO_4 and NH_3H_2O solutions by electrochemical methods and surface analysis, Mater. Chem. Phys. 93 (2005) 429. DOI: 10.1016/j.matchemphys.2005.03.049.

[19] T. Mayer, M. Lebedev, R. Hunger, W. Jaegermann, Elementary processes at semiconductor/electrolyte interfaces: perspectives and limits of electron spectroscopy, Appl. Surf. Sci. 252 (2005) 31. DOI: 10.1016/j.apsusc.2005.01.110.

[20] M. V. Lebedev, T. Masuda, K. Uosaki, Charge transport at the interface of n-GaAs (100) with an aqueous HCl solution: electrochemical impedance spectroscopy study, Semicond. 46 (2012) 471. DOI: 10.1134/S1063782612040136.

[21] B. H. Erné, F. Ozanam, J. -N. Chazalviel, Dynamics of hydrogen adsorption on GaAs electrodes, Phys. Rev. Lett. 80 (1998) 4337. DOI: 10.1103/PhysRevLett.80.4337.

[22] R. Memming, Semiconductor electrochemistry, Wiley-VCH , Darmstadt, 2001.

[23] N. Sato, Electrochemistry at metal and semiconductor electrodes, Elsevier Science B.V., Amsterdam, 1998.

[24] G. Oskam, P. M. Hoffmann, A. Natarajan, P. C. Searson, Semiconductor/electrolyte boundaries, in: J. G. Webster, Wiley Encyclopedia of electrical and electronics engineering, John Wiley and Sons, 2007. DOI: 10.1002/047134608X.W3225.pub2.

[25] M. Palomar-Pardavé, M. Miranda-Hernández, I. González, N. Batina, Detailed characterization of potentiostatic current transients with 2D-2D and 2D-3D nucleation transitions, Surf. Sci. 399 (1998) 80. DOI: 10.1016/S0039-6028(97)00813-3.

[26] M. H. Hölzle, U. Retter, D. M. Kolb, The kinetics of structural changes in Cu adlayers on Au(111), J. Electroanal. Chem. 371 (1994) 101. DOI: 10.1016/0022-0728(93)03235-H.

[27] M. Palomar-Pardavé, B. Scharifker, E. Arce, M. Romero-Romo, Nucleation and diffusion-controlled growth of electroactive centers. Reduction of protons during cobalt electrodeposition, Electrochim. Acta 50 (2005) 4736. DOI: 10.1016/j.electacta.2005.03.004.

[28] B. H. Erné, M. Stchakovsky, F. Ozanam, J.-N. Chazalviel, Surface composition of n-GaAs cathodes during hydrogen evolution characterized by in situ ultraviolet-visible ellipsometry and in situ infrared spectroscopy, J. Electrochem. Soc. 145 (1998) 447. DOI: 10.1149/1.1838283.

[29] P. M. Rigano, C. Mayer, T. Chierchie, Electrochemical nucleation and growth of copper on polycriystalline palladium, J. Electroanal. Chem. Interfacial Electrochem. 248 (1988) 219. DOI: 10.1016/0022-0728(88)85163-5.

[30] B. R. Scharifker, J. Mostany, M. Palomar-Pardavé, I. González, On the theory of the potentiostatic current transient for diffusion-controlled three-dimensional electrocrystallization processes, J. Electrochem. Soc. 146 (1999) 1005. DOI: 10.1149/1.1391713.

[31] P. M. Vereecken, P. C. Searson, Electrochemical deposition of Bi on GaAs (100), J. Electrochem. Soc. 148 (2001) C733. DOI: 10.1149/1.1406493.

[32] I. Uhlendorf, R. Reineke-Koch, R. Memming, Analysis of the hydrogen formation at GaAs electrodes by impedance spectroscopy investigations, Ber. Bunsenges. Phys. Chem. 99 (1995) 1082. DOI: 10.1002/bbpc.199500038.

[33] E. H. Rhoderick, Metal-semiconductor contacts, IEE Proceedings I - Solid-State and Electron Devices 129 (1982) 1. DOI: 10.1049/ip-i-1.1982.0001.

[34] Y. A. Goldberg, E. A. Posse, B. V. Tsarenkov, Mechanism of flow of direct current in GaAs surface-barrier structures, Sov. Phys. Semicond. 9 (1975) 337.

[35] W. E. Spicer, Z. Liliental-Weber, E. Weber, N. Newman, T. Kendelewicz, R. Cao, C. McCants, P. Mahowald, K. Miyano, I. Lindau, The advanced unified defect model for Schottky barrier formation, J. Vac. Sci. Tec. B 6 (1988) 1245. DOI: 10.1116/1.584244.

[36] J. S. Blakemore, Approximation for Fermi-Dirac Integrals, especially the function F_1/2(η) used to describe electron density in a semiconductor, Solid-State Electron. 25 (1982) 1067. DOI: 10.1016/0038-1101(82)90143-5.

[37] S. M. Sze, Physics of Semiconductor Devices, John Wiley & Sons, Inc., New York, 1981.

[38] V. L. Rideout, C. R. Crowell, Effects of image force and tunneling on current transport in metal-semiconductor (Schottky barrier) contacts, Solid-State Electron. 13 (1970) 993. DOI: 10.1016/0038-1101(70)90097-3.

[39] A. M. Cowley, S. M. Sze, Surface states and barrier height of metal semiconductor Systems, J. Appl. Phys. 36 (1965) 3212. DOI: 10.1063/1.1702952.

[40] W. Mönch, Electronic structure of metal-semiconductor contacts, Springer, Dordrecht, 1990.

[41] R. Stratton, Volt-current characteristics for tunneling through insulating films, J. Phys. Chem. Sol. 23 (1962) 1177. DOI: 10.1016/0022-3697(62)90165-8.

[42] J. R. Taylor, An introduction to error analysis. The study of uncertainties in physical measurements, University Science Books, Sausalito (CA - USA), 1997.

[43] K. Rajeshwar, T. Mraz, The n-GaAs/electrolyte interface: evidence for specificity in lattice ion-electrolyte interactions, dependence of interfacial potential drops on crystal plane orientation to the electrolyte and implications for solar energy conversion, J. Phys. Chem. 87 (1983) 742. DOI: 10.1021/j100228a010.

[44] P. Allongue, E. Souteyrand, L. Allemand, Metal electrodeposition on semiconductors. Part III: Description of charge transfer for the formation of Schottky diodes, J. Electroanal. Chem. 362 (1993) 89. DOI: 10.1016/0022-0728(93)80009-7.

[45] L. M. Depestel, K. Strubbe, Influence of the crystal orientation on the electrochemical behaviour of n-GaAs in Au(I)-containing solutions, Phys. Chem. Chem. Phys. 5 (2003) 2881. DOI: 10.1039/B302243A.

[46] H. Lüth, Surface and interfaces of solid materials, Springer, Berlin, 1995. DOI 10.1007/978-3-662-03132-2.

[47] P. Allongue, Steady state photocapacitance study of semiconductor/electrolyte junctions II. Surface state distribution and charge transfer mechanisms, Ber. Bunsenges. Phys. Chern. 92 (1988) 895. DOI: 10.1002/bbpc.198800217.

[48] M. S. Antelman, The encyclopedia of chemical electrode potentials (1st ed.), Plenum Press, New York, 1982. DOl: 10.1007/978-1-4613-3374-6.

[49] S. Trassati, Work function, electronegativity, and electrochemical behaviour of metals. III. Electrolytic hydrogen evolution in acid solutions, Electroanal. Chem. Interf. Electrochem. 39 (1972) 163. DOI: 10.1016/S0022-0728(72)80485-6.

[50] S. H. Cadle, S. Bruckenstein, Ring-disk electrode study of the reduction of bismuth on platinum, Anal. Chem. 44 (1972) 1993. DOI: 10.1021/ac60320a011.

[51] P. M. Vereecken, K. Rodbell, C. Ji, P. C. Searson, Electrodeposition of bismuth thin films on n-GaAs (110), Appl. Phys. Lett. 86 (2005) 121916. DOI: 10.1063/1.1886248g.

[52] M. A. Elmorsi, K. Jüttner, Electrolytic deposition of bismuth on CdS(0001) single-crystal surfaces, Electrochim. Acta 31 (1986) 211. DOI: 10.1016/0013-4686(86)87110-9.

[53] M. Palomar-Pardavé, J. Aldana-González, L. E. Botello, E. M. Arce-Estrada, M. T. Ramírezz-Silva, J. Mostany, M. Romero-Romo, Influence of temperature on the

thermodynamics and kinetics of cobalt electrochemical nucleation and growth, Electrochim. Acta 241 (2017) 162. DOI: 10.1016/j.electacta.2017.04.126.

[54] E. Barrera, M. Palomar-Pardavé, N. Batina, I. González, Formation mechanisms and characterization of black and white cobalt electrodeposition onto stainless steel, J. Electrochem. Soc. 147 (2000) 1787. DOI: 10.1149/1.1393435.

[55] M. Aguilar-Sánchez, M. Palomar-Pardavé, M. Romero-Romo, M. T. Ramírez-Silva, E. Barrera, B. R. Scharifker, Electrochemical nucleation and growth of black and white chromium deposits onto stainless steel surfaces, J. Electroanal. Chem. 647 (2010) 128. DOI: 10.1016/j.jelechem.2010.06.012.

[56] P. Sebastián, L. E. Botello, E. Vallés, E. Gómez, M. Palomar-Pardavé, B. R. Scharifker, J. Mostany, Three-dimensional nucleation with diffusion controlled growth: A comparative study of electrochemical phase formation fromaqueous and deep eutectic solvents, J. Electroanal. Chem. 793 (2017) 119. DOI: 10.1016/j.elechem.2016.12.014.

[57] M. Enache, C. Negrila, M. Anastasescu, G. Dobrescu, M. F. Lazarescu, V. Lazarescu, Surface states- and field-effects at GaAs(100) electrodes in sodium dodecyl sulfate acid solution, J. Electrochem. Soc. 165 (2018) H3008. DOI: 10.1149/2.0031804jes.

[58] L. J. J. Janssen, J. Hoogland, The effect of electrolytically evolved gas bubbles on the thickness of the diffusion layer, Electrochim. Acta 15 (1970) 1013. DOI: 10.1016/0013-4686(73)85016-9.

[59] N. D. Nikolić, K. I. Popov, L. J. Pavlović, M. G. Pavlović, The effect of hydrogen codeposition on the morphology of copper electrodeposits. I. The concept of effective overpotential, J. Electroanal. Chem. 588 (2006) 88. DOI: 10.1016/j.jelechem.2005.12.006.

[60] H.-C. Shin, J. Dong, M. Liu, Nanoporous structures prepared by an electrochemical deposition process, Adv. Mater. 15 (2003) 1610. DOI: 10.1002/adma.200305160.

[61] K. Msellak, J. -P. Chopart, O. Jbara, O. Aaboubi, J.Amblard, Magnetic field effects on Ni–Fe alloys codeposition, J. Magn. Magn Mater. 281 (2004) 295. DOI: 10.1016/j.jmmm.2004.04.118

[62] A. Llavona, L. Pérez, M. Sánchez, V. de Manuel, Enhancement of anomalous codeposition in the synthesis of Fe–Ni alloys in nanopores, Electrochim. Acta 106 (2013) 392. DOI: 10.1016/j.electacta.2013.05.116.

[63] A. De Vrieze, K. Strubbe, W. P. Gomes, S. Forment, R. L. Van Meirhaeghe, Electrochemical formation and properties of n-GaAs/Au and n-GaAs/Ag Schottky barriers: Influence of surface composition upon the barrier height., Phys. Chem. Chem. Phys. 3 (2001) 5297. DOI: 10.1039/b104887m.

FIGURES CAPTIONS

Figure 1. Cyclic voltammetry scans performed on a lower-doped n-GaAs(111)B substrate into the Bi(III) solution at 10 mV/s.

Figure 2. (a) Current density transients recorded during the nucleation of the Bi layers electrodeposited on lower-doped n-GaAs(111)B substrates at different overpotentials. Individual contributions obtained from the deconvolution of the transient recorded at a η_{SEI} of (b) -0.32 V, (c) -0.37 V, (d) -0.52 V, and (e) -0.77 V. Insets: enlargement of the initial current density decay.

Figure 3. AFM images and representative depth profiles shown below each image measured on the Bi thin films (40 nm) grown on lower-doped n-GaAs(111)B substrates at a η_{SEI} of (a) -0.32 V, (b) -0.37 V, (c) -0.52 V, (d) -0.77 V, and (e) performing several CV scans.

Figure 4. Bragg–Brentano XRD patterns of the Bi films grown on lower-doped n-GaAs(111)B substrates at different η_{SEI} (static mode) and performing CV scans (dynamic mode). The dashed lines indicate the position of Bi reflections (ICDD card 00-044-1246) that matches with an observed peak. Peaks marked with * correspond to GaAs(333) reflections.

Figure 5. FWHM of ω-rocking and ϕ-scans measured in the Bi films.

Figure 6. (a) Experimental *j*-*V* curves measured in the Bi films. (b) Experimental *j*-*V* curves measured in the films grown at η_{SEI} = -0.37 V and -0.77 V with their corrresponding fittings.

Figure 7. Energy band diagram at OCP conditions of a SEI formed by an n-GaAs substrate ($n = 1.3 \cdot 10^{17}$ cm^{-3}) immersed in the Bi(III) solution.

FIGURES

Graphical Abstract

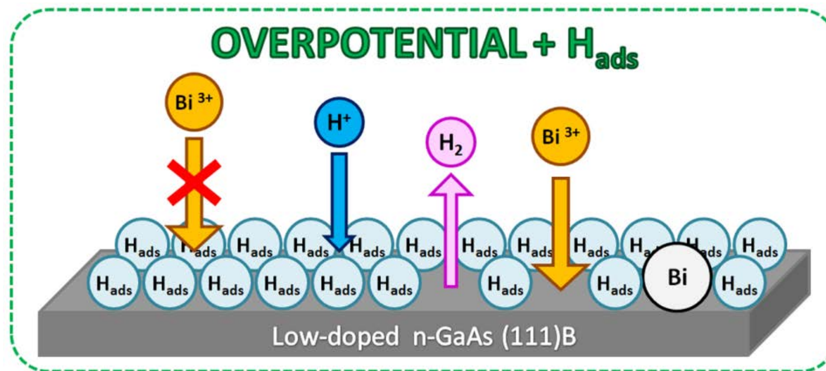

Figure 1

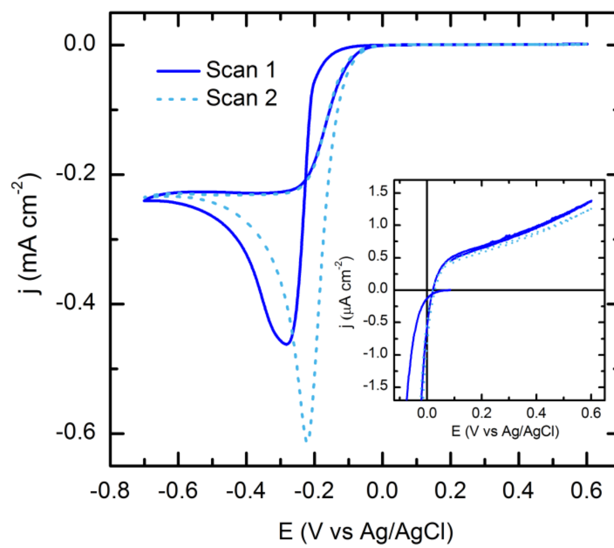

Figure 2

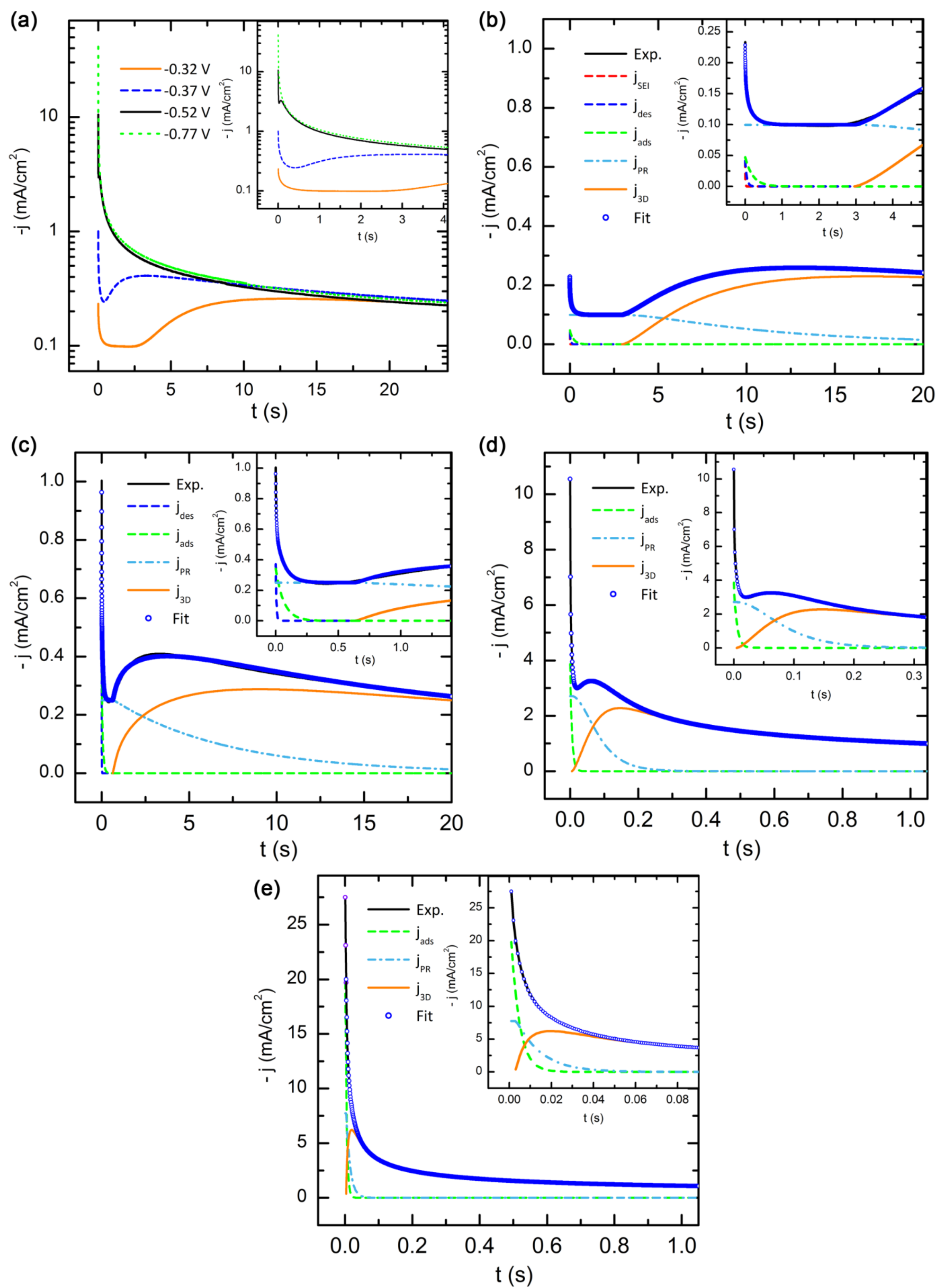

Figure 3

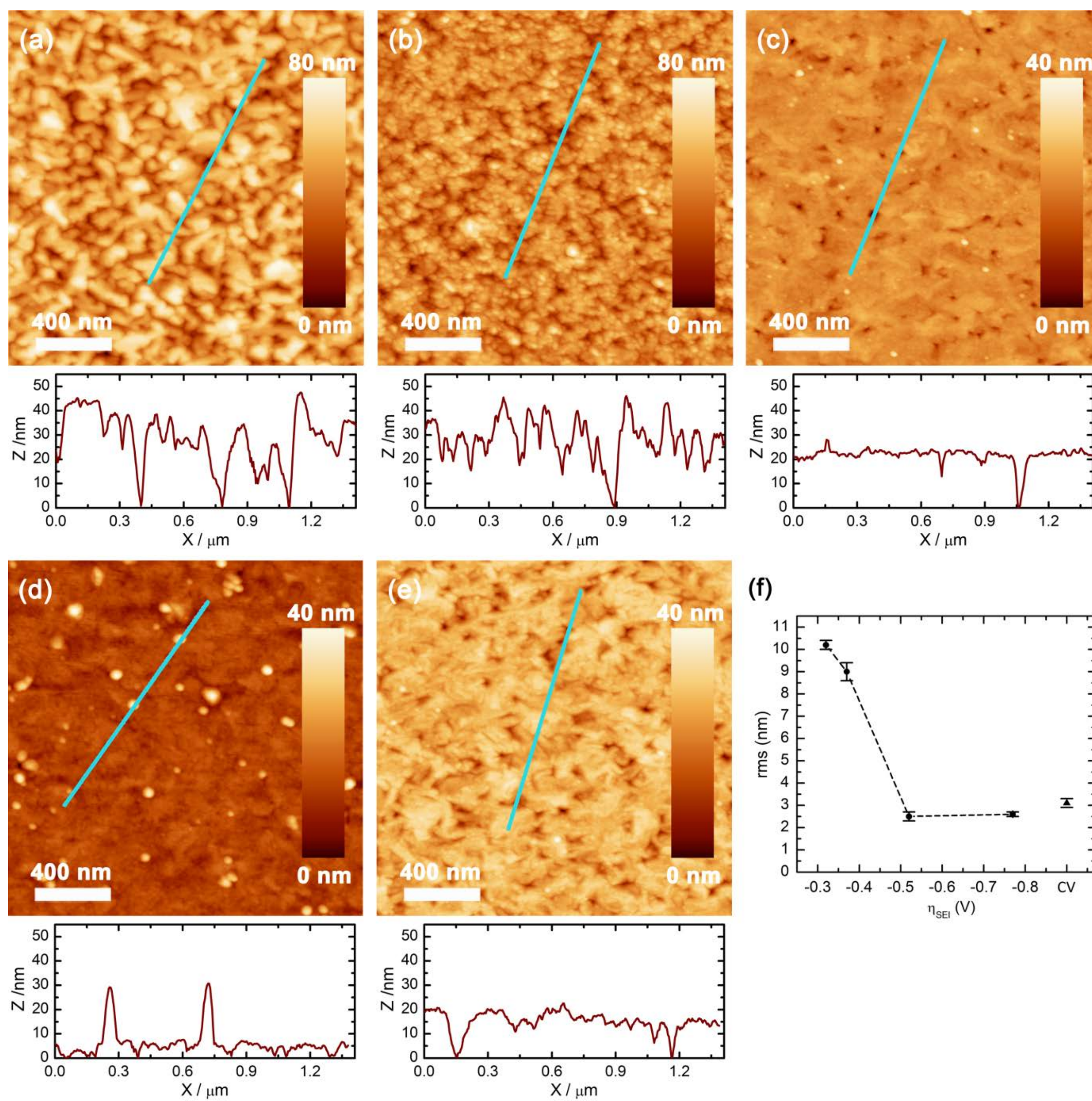

Figure 4

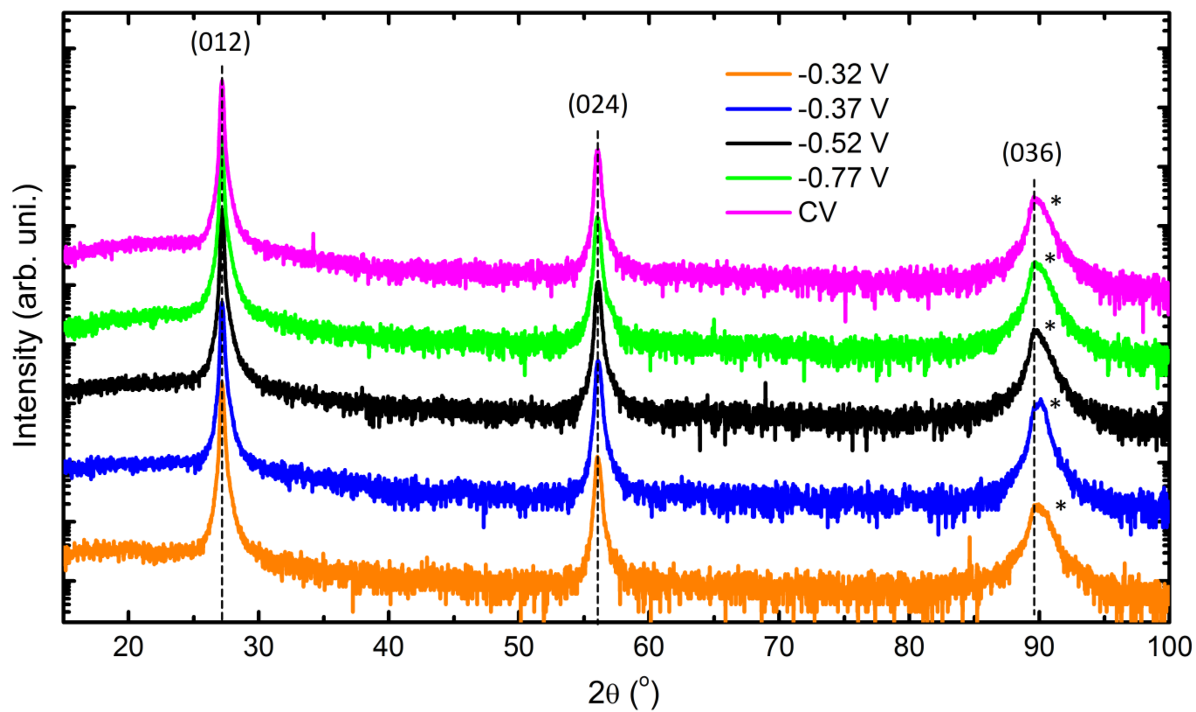

Figure 5

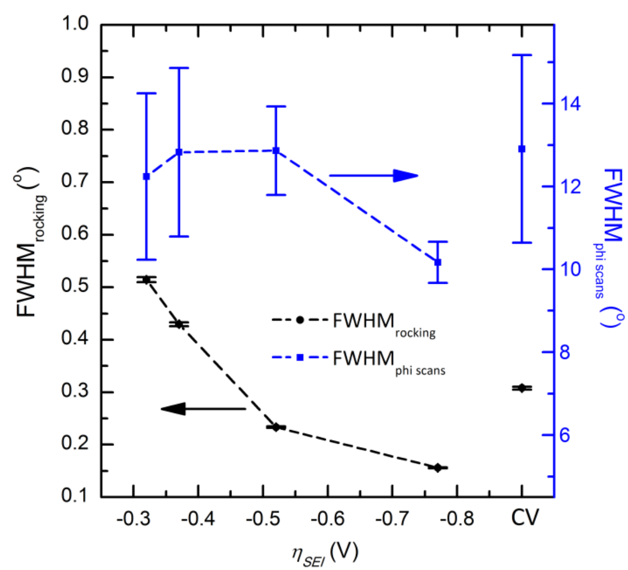

Figure 6

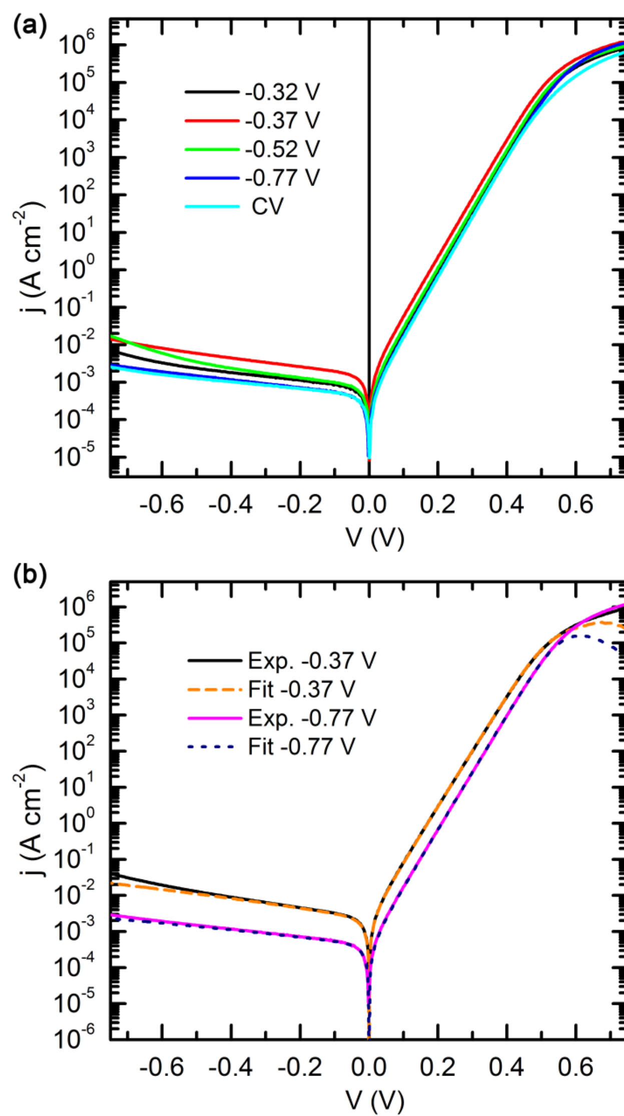

Figure 7